The Initiation of Modern "Soft Snowball" and "Hard Snowball" Climates in CCSM3. Part II: Climate Dynamic Feedbacks

JUN YANG

Department of Physics, University of Toronto, Toronto, Ontario, Canada, and Laboratory for Climate and Ocean-Atmosphere Studies, Department of Atmospheric and Oceanic Sciences, School of Physics, Peking University, Beijing, China

W. RICHARD PELTIER

Department of Physics, University of Toronto, Toronto, Ontario, Canada

YONGYUN HU

Laboratory for Climate and Ocean-Atmosphere Studies, Department of Atmospheric and Oceanic Sciences, School of Physics, Peking University, Beijing, China

(Manuscript received 1 April 2011, in final form 27 September 2011)

ABSTRACT

This study investigates the climate dynamic feedbacks during a transition from the present climate to the extremely cold climate of a "Snowball Earth" using the Community Climate System Model, version 3 (CCSM3). With the land–sea distribution fixed to modern, it is found that by reducing solar luminosity and/or carbon dioxide concentration: 1) the amount of atmospheric water vapor and its attendant greenhouse effect decrease with the logarithm of sea ice cover, thereby promoting the expansion of sea ice; 2) over the sea ice, the cloud radiative feedback is positive, thus enhancing sea ice advance; over the ocean, the cloud radiative feedback is first negative and then becomes positive as sea ice enters the tropics; and 3) the strength of the atmospheric Hadley cell and the wind-driven ocean circulation increases significantly in the Southern Hemisphere, inhibiting the expansion of sea ice into the tropics. Meanwhile, the North Atlantic Deep Water cell disappears and the Antarctic Bottom Water cell strengthens and expands to occupy almost the entire Atlantic basin. In the experiment with 6% less solar radiation and 70 ppmv CO_2 compared to the control experiment with 100% solar radiation and 355 ppmv CO_2 near the ice edge (28°S latitude), the changes of solar radiation, CO_2 forcing, water vapor greenhouse effect, longwave cloud forcing at the top of the model, and atmospheric and oceanic energy transport are -22.4, -6.2, -54.4, $+6.2$, and $+16.3$ W m^{-2}, respectively. Therefore, the major controlling factors in producing global ice cover are ice albedo feedback (Yang et al., Part I) and water vapor feedback.

1. Introduction

In the companion paper, Yang et al. (2012, hereafter Part I), the forcing required for the present-day earth to enter a state of complete glaciation was investigated using the Community Climate System Model, version 3 (CCSM3). It was found that runaway glaciation would occur as a 6% reduction in solar radiation with 17.5–20 ppmv CO_2 or a 10%–10.5% reduction in solar radiation with 286 ppmv CO_2. The required forcings were found to be very sensitive to the assumed values of sea ice and snow albedos. Furthermore, we demonstrated the existence of soft Snowball solutions, in which the sea ice margins may extend to 10°S (N) latitudes, tropical open water oceans stably coexists with year-round snow-covered tropical continents, and runaway albedo feedback does not occur. The current study continues the analysis of the simulations described in Part I by examining the detailed climate dynamical processes involved in the transition from the present-day climate to an "ice house" state of the Neoproterozoic, including water vapor feedback, cloud radiative feedback, sea ice

Corresponding author address: Jun Yang, 40 Gerrard Street East, Apt. 3308, Toronto ON M5B 2E8, Canada.
E-mail: jyangdas@atmosp.physics.utoronto.ca

DOI: 10.1175/JCLI-D-11-00190.1

thermodynamics and dynamics, atmospheric and oceanic circulations, and meridional energy transports.

Climate models of various levels of sophistication have been employed to investigate the issue of the initiation of a Snowball Earth, including energy balance models (Bendtsen 2002; Tajika 2003; Rose and Marshall 2009; Roe and Baker 2010; Pierrehumbert et al. 2011), ice sheet coupled energy balance climate models (Hyde et al. 2000; Crowley et al. 2001; Peltier et al. 2007; Liu and Peltier 2010, 2011), 1D ''flowing'' sea glacier models (Goodman and Pierrehumbert 2003; Pollard and Kasting 2005; Goodman 2006), atmospheric general circulation models coupled to a mixed layer ocean (Jenkins and Smith 1999; Hyde et al. 2000; Chandler and Sohl 2000; Baum and Crowley 2001; Romanova et al. 2006; Micheels and Montenari 2008; Pierrehumbert et al. 2011), earth climate system models of intermediate complexity (Donnadieu et al. 2004b; Lewis et al. 2003, 2007), and fully coupled ocean–atmosphere models (Poulsen et al. 2001, 2002; Peltier et al. 2004; Poulsen and Jacob 2004; Voigt and Marotzke 2010; Voigt et al. 2011; Part I). The following five statements are generally agreed on based on the results of the above-mentioned models. 1) The CO_2 threshold required for the onset of a hard Snowball Earth (completely ice-covered continents and oceans) is strongly sensitive to the surface sea ice/snow albedo parameterizations (Pierrehumbert et al. 2011; Part I). 2) The tropical wind-driven oceanic circulations, which transport heat poleward, are able to weaken the influence of ice albedo feedback (Lewis et al. 2003; Poulsen and Jacob 2004; Donnadieu et al. 2004b; Voigt and Marotzke 2010). 3) The role of the Hadley cells (HCs) is time dependent: so long as sea ice remains poleward of the tropics, the HCs transport relatively warm air from the tropics to the subtropics and thus inhibit the influence of ice albedo feedback, but once the sea ice enters into the domain of the HCs, the near-surface branch of the HCs transports relatively cold air from the subtropics to the sea ice fronts in both hemispheres and thus enhances the ice albedo feedback (Bendtsen 2002; Poulsen and Jacob 2004; Voigt and Marotzke 2010). 4) The land ice sheets, growing at mid- and high latitudes, are able to flow to low latitudes and then cover the tropical continents, implying that the inferred ice sheets of the tropics may not have developed in situ (Hyde et al. 2000; Pollard and Kasting 2004; Peltier et al. 2007; Liu and Peltier 2010, 2011). 5) Sea ice dynamics has important impacts on the initiation of the Snowball Earth (Lewis et al. 2007; Part I), as well as sea glacier dynamics (Goodman and Pierrehumbert 2003; Pollard and Kasting 2005; Goodman 2006).

Despite the volume of work that has been accumulating on this topic, there remain several important issues that are not entirely clear. First, what is the sign of cloud radiative feedback, negative or positive? Our analysis of the CCSM3 results shows that over the sea ice, the high-level cloud fraction decreases and the low-level cloud fraction increases, resulting in a positive cloud feedback and thereby promoting the equatorward advance of the sea ice, while over the open oceans, the cloud radiative feedback is first negative and then positive as the sea ice enters the tropics (section 3c). Moreover, there have been some misleading comparisons in cloud forcings between the Fast Ocean Atmosphere Model (FOAM) and the ECHAM5/Max Planck Institute Ocean Model (MPI-OM). Poulsen and Jacob (2004) found that the net cloud forcing (NCF, shortwave plus longwave) over the sea ice in FOAM to be as high as $+30$ W m^{-2}, while Voigt and Marotzke (2010) pointed out that NCF in ECHAM5/MPI-OM is close to zero. In the analysis of Poulsen et al. (2001, 2002) and Poulsen and Jacob (2004), the authors calculated the NCF at the surface (NCF_SRF) (C. J. Poulsen 2011, personal communication), while Voigt and Marotzke (2010) computed NCF at the top of the model (NCF_TOM); in the control run of CCSM3, we find that at high latitudes NCF_TOM is 29 W m^{-2} less than NCF_SRF, whereas in the tropical region NCF_TOM is 15 W m^{-2} larger than NCF_SRF. Thus, NCF_TOM and NCF_SRF must be discussed separately. Herein, we will present the cloud radiative forcings both at TOM and at SRF in CCSM3 and compare them with ECHAM5/MPI-OM and FOAM.

A second important issue that remains outstanding concerns the sign of atmospheric circulation feedback, especially for the tropical Hadley cells. It is clear that the strength of the Hadley cells will increase significantly as sea ice spreads toward the tropics due to the increased meridional temperature gradient (Poulsen and Jacob 2004; Voigt and Marotzke 2010); this effect is also found in CCSM3. However, Poulsen and Jacob (2004) and Voigt and Marotzke (2010) concluded that as the sea ice becomes very close to the equator, the Hadley cells largely weaken or entirely collapse because they found that the strength of ''annual mean'' Hadley cells abruptly decreases prior to the final onset of global ice cover. This is a misleading notion in our view. Based on a more detailed analysis of the seasonal cycle of the HCs, we find, and will discuss in detail in what follows, that as the sea ice approaches the equator, the Hadley cells exhibit an extremely strong seasonal cycle and cancel each other between different months, owing to the low thermal inertia of the surface; although the annual-mean pattern becomes very weak, during most of the year, especially at the times of the solstices, the Hadley cells are still exceptionally strong and transport very large amounts of energy from the summer hemisphere to the winter hemisphere and thus act to homogenize the tropical

temperature field and promote sea ice advance (for further details, see section 3e).

A third important issue concerns the response of the tropical wind-driven oceanic circulations (WDOCs) to ''Snowball'' onset. When the sea ice is outside of the tropics, both the wind-driven cells and the Hadley cells transport heat poleward and weaken the influence of ice albedo feedback. However, as the sea ice enters into the domain of the Hadley cells, the influence of the wind-driven oceanic circulations opposes that of the atmospheric Hadley cells; the WDOCs act to maintain the heat transport from the equator to the sea ice fronts and therefore promote sea ice melting, while the Hadley cells promote the growth of the sea ice as described previously. Moreover, the strength of the wind-driven circulations increases as the sea ice advances equatorward (Donnadieu et al. 2004b; Poulsen and Jacob 2004; Voigt and Marotzke 2010). We address in greater detail the feedback of the wind-driven circulations in CCSM3 in section 3f.

A fourth, and as we will show, extremely interesting issue of the Snowball transition, concerns the response of the thermohaline circulation. On the one hand, the equatorward advance of the sea ice decreases the meridional gradient of ocean temperature and cuts off the driving force of the surface winds over the ocean, both of which serve to weaken the thermohaline circulation; on the other hand, at high latitudes, high-salinity water produced by sea ice formation is injected into the ocean and thereby enhances the thermohaline circulation (Peltier et al. 2004; Donnadieu et al. 2004b). All of these changes may serve to dramatically modify the thermohaline circulation from its present-day form (section 3g).

The fifth and final issue to be addressed herein concerns the response of atmospheric and oceanic energy transports. The energy transports affect the equator-to-pole temperature gradient ΔT; high ΔT makes it easier to grow ice sheets and sea ice at mid- and high latitudes and thereby enhances ice albedo feedback, and vice versa (Pierrehumbert 2002). On the present earth, both observations and theoretical analysis suggest that in the tropical region, the oceanic energy transport and the atmospheric energy transport are comparable, and that the ocean component dominates the energy transport in the deep tropics; in the midlatitudes, the atmospheric circulation explains about 80% of the total energy transport, with the oceanic circulation contributing the remainder (Trenberth and Caron 2001; Held 2001; Czaja and Marshall 2006). However, under the extreme cold climate conditions of the ''Snowball Earth,'' as we discuss, the situation is quite different. We will systematically analyze the modification of the total equator-to-pole energy transport and the contributions by different processes in response to reductions in solar radiation and/or CO_2 concentration (see section 3h).

The purpose of this paper is to address the five issues described above. Here, we will describe the implications of a series of 16 experiments to provide a clear understanding of the transition from the current climate to extremely cold climates. The paper is organized as follows. Section 2 briefly describes CCSM3 and the design of the experiments. Section 3 reports the results. We also compare our results with those obtained previously using FOAM and ECHAM5/MPI-OM (Poulsen and Jacob 2004; Voigt and Marotzke 2010), especially for the cloud radiative forcing and meridional energy transports. Section 4 presents a discussion of our results, and section 5 offers a summary of our conclusions.

2. Model description and experimental design

As in Part I, the model used in this investigation is a fully coupled atmosphere–ocean–land–sea ice model, the National Center of Atmospheric Research's (NCAR) CCSM3. For more details, please see Part I as well as Collins et al. (2006b) and the references therein. Here, the main features of the model are simply highlighted.

The atmospheric module of CCSM3 is based upon an Eulerian spectral dynamical core with triangular spectral truncation at 31 wavenumbers and 26 vertical levels from the surface to approximately 2.0 hPa. The land module [Community Land Model, version 3 (CLM3)] is integrated on the same horizontal grid as the atmosphere, and each grid cell is further divided into a hierarchy of land units, soil columns, and plant function types. The ocean module is based upon the Parallel Ocean Program version 1.4.3 with the vertical structure defined on 25 levels extending to 4.75-km depth. The sea ice module [Community Sea Ice Model version 5 (CSIM5)] includes both energy conserving thermodynamics and elastic–viscous–plastic dynamics.

As in the first stage of this work, we employ the geography and topography of the present-day earth. The results of these analyses will also be beneficial for the next step in this new sequence of analyses that will be based on the implementation of more realistic Neoproterozoic geography, since the comparison of the results with those to be described herein will provide a means of isolating the influence of the continent–ocean configuration. Based on our analyses, we will provide a brief discussion of what we expect will be the influence of paleogeography on the results.

At ~600 Ma (Ma = million years ago), the solar luminosity was 6%–7% less than the present, while the CO_2 concentration is unknown. We have carried out a sequence of simulations by abruptly decreasing the solar

TABLE 1. Brief summary of the CCSM3 simulations employed in this paper.

Groups	Runs	Description
Control run	1	Solar constant is 1367 W m^{-2}. CO_2 level is fixed at 355 ppmv. Integration time is 800 model years.
Reduced solar radiation	9	CO_2 level is fixed at 286 ppmv. Solar radiation is 99%, 98%, 97%, 96%, 95%, 94%, 92%, 89.5%, or 88% of the present level. Integration time is 3000, 3000, 3000, 3000, 3000, 3000, 1600, 350, or 700 yr, respectively.
Reduced CO_2 level	6	Solar radiation is fixed at 94% of the present level. CO_2 concentration is 140, 70, 50, 35, 25, or 17.5 ppmv. Integration time is 1000, 1500, 800, 1600, 700, or 450 yr, respectively.

constant and/or CO_2 concentration from the values appropriate to the modern control climate. The solar luminosity was varied through the sequence of 100%–88% of the present level in steps of 1% or 2%, and the CO_2 level was fixed to a member of the sequence 286, 140, 70, 50, 35, 25, or 17.5 ppmv (Table 1). Other atmospheric greenhouse gases are fixed at the preindustrial levels, CH_4 = 805.6 ppbv, N_2O = 276.7 ppbv, and no chlorofluorocarbons (CFCs), except for the control experiment with 100% solar radiation, in which the greenhouse gases are fixed at the present-day level (355 ppmv CO_2, 1714.0 ppbv CH_4, and 311.0 ppbv N_2O). A zonally symmetric latitude–height distribution of ozone is specified, corresponding to the monthly-mean climatology under the present-day conditions. In these experiments, when the surface air temperature T_S is equal to or below −1°C, the sea ice albedo and snow albedo are 0.50 and 0.78, respectively; as T_S increases to 0°C, the sea ice albedo and snow albedo are assumed to be 0.425 and 0.656, respectively. The orbital parameters are fixed to the present-day values. All of the experiments to be analyzed herein were initiated from a present-day statistical equilibrium climate, and most of the simulations were integrated for as many as 3000 yr. The last 100 yr of each experiment are employed for the purpose of the analyses to be described herein. For further details concerning this master set of experiments, please see Part I.

3. Results

a. *Overview of the thermal structure of the atmosphere and ocean*

Annual- and zonal-mean sea ice cover, surface air temperature, and precipitation are illustrated in Fig. 1. In the control experiment (100% solar radiation of 1367 W m^{-2} and 355 ppmv CO_2), the global-mean surface air temperature is 287.1 K and the global-mean sea ice coverage is approximately 6%. By reducing either solar radiation or CO_2 concentration, the sea ice advances equatorward, the precipitation rate decreases, and the global-mean surface air temperature declines quasi linearly at the rate of 0.78 K $(W\ m^{-2})^{-1}$. For a CO_2 volume mixing ratio between 50 and 20 ppmv, the sea ice enters the tropics and stabilizes without evolving into a state of total glaciation and the sea ice fronts stabilize within the range of 30°–10°S (N). As CO_2 decreases to 17.5 ppmv, however, the ice albedo instability occurs and the global-mean surface temperature declines to less than −36°C as the system enters the hard Snowball state of complete ice/snow cover.

Figure 1c indicates that the location of the intertropical convergence zone (ITCZ) changes significantly with reductions in solar radiation and/or CO_2 concentration, which is a consequence of a modified interhemispheric temperature gradient (Broccoli et al. 2006). In the experiments with 99%–96% solar radiation and 286 ppmv CO_2, T_S decreases in both hemispheres but the decrease of T_S in the Northern Hemisphere (NH) is about 6 K greater than in the Southern Hemisphere (SH) (Fig. 1b) because of the significant weakening or termination of the North Atlantic meridional overturning circulation (NAMOC) (see Fig. 13), and thereby the location of the ITCZ shifts southward about 3° in latitude (Fig. 1c). In the experiments with 94% solar radiation and 70–25 ppmv CO_2, however, the decrease in T_S in the SH is greater than in the NH because of the relatively fast advance of the sea ice in the SH (Fig. 1a), as a result the ITCZ shifts from the SH to the NH.

Annual-mean cross sections of zonally averaged ocean potential temperature are shown in Fig. 2. After reducing the solar radiation and/or CO_2 concentration, the ocean surface temperatures decrease mostly through infrared radiation and sensible heat loss to the atmosphere; for the underlying water column, vertical convective mixing transfers heat from deeper levels to the surface, cooling the deep water (Poulsen et al. 2001). For example, with a 6% reduction in solar radiation with 70 ppmv CO_2 (Fig. 2i), only in the region between ~30°S and 30°N and above 500 m is the ocean water temperature higher than 0°C. Although this region occupies only approximately 6% of the entire ocean volume, it includes approximately 60% of the area of the ocean surface. In

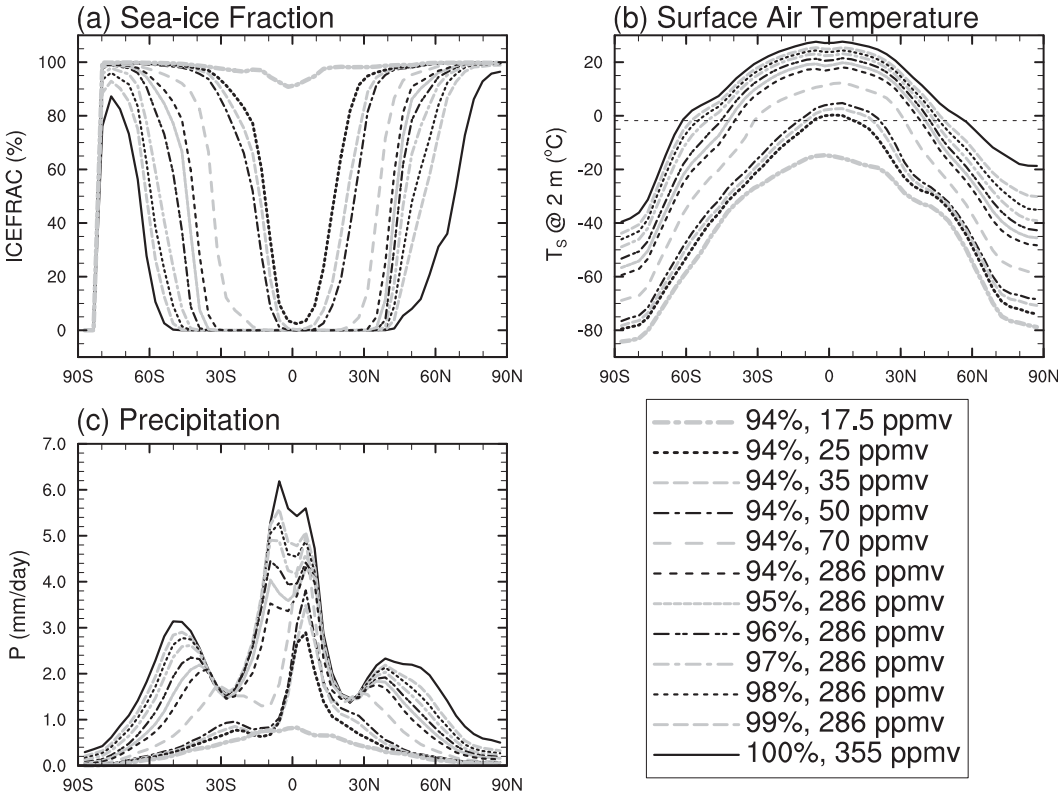

FIG. 1. Annual- and zonal-mean (a) sea ice cover, (b) surface air temperature, and (c) precipitation in the experiments with different solar radiations and CO_2 concentrations.

this same sequence of analyses, the height of the atmospheric tropopause and the depth of the permanent thermocline significantly decrease (Fig. 3). On a hard Snowball Earth, all of the ocean surface is covered by sea ice and the entire ocean potential temperature is nearly uniform, between 0° and −1.8°C (the freezing point) (not shown).

b. *Water vapor feedback*

For clear-sky greenhouse effect G, following Pierrehumbert (2004, 2005), this can be approximately defined as $G \equiv \sigma T_S^4 - \mathrm{OLR}_{\mathrm{clear}}$, where σ is the Stefan–Boltzmann constant, T_S is the surface temperature, and $\mathrm{OLR}_{\mathrm{clear}}$ is clear-sky outgoing longwave radiation at the

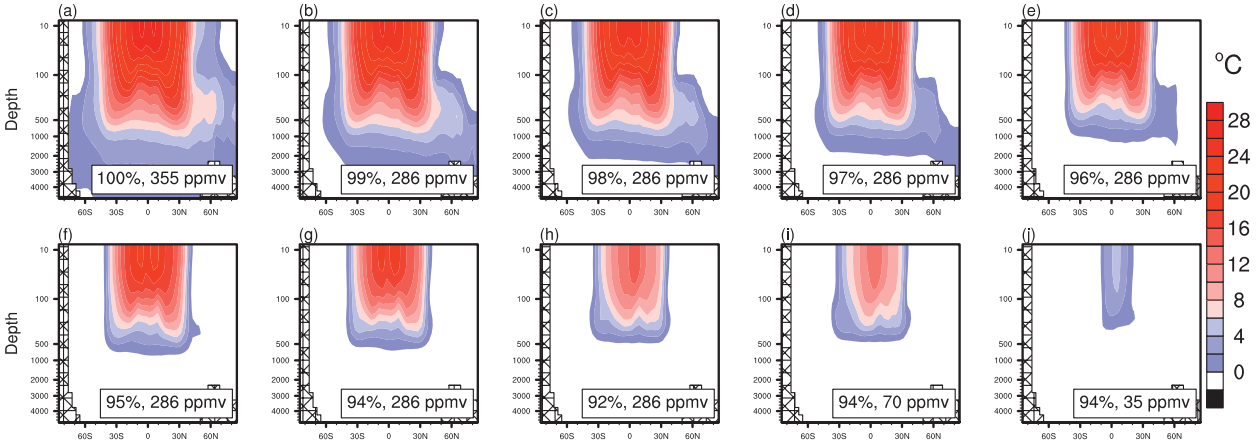

FIG. 2. Annual- and zonal-mean ocean potential temperature in the experiments with different solar radiations and CO_2 concentrations. Solar radiation percentage and carbon dioxide concentration are marked in each panel.

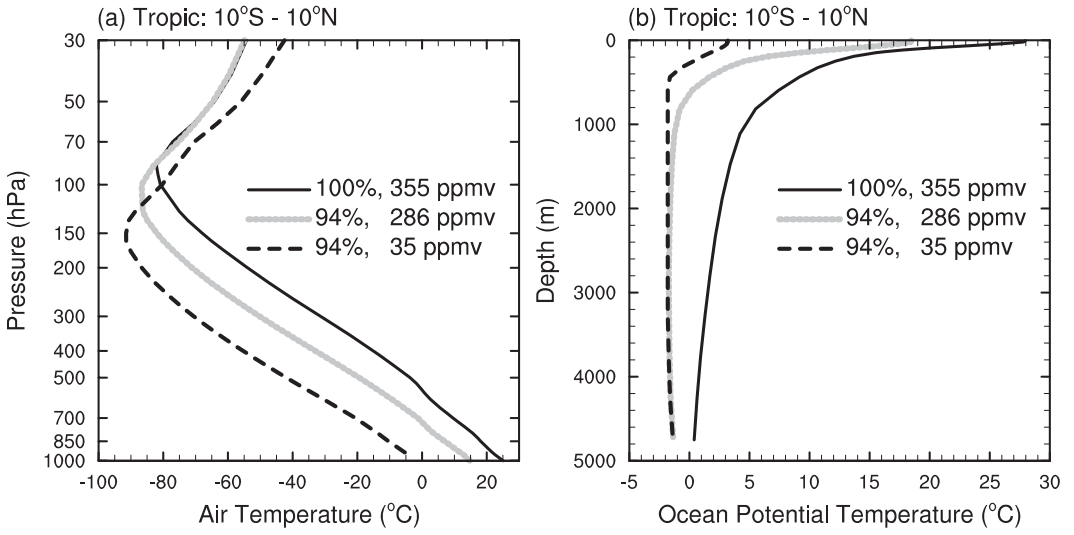

FIG. 3. Annual- and zonal-mean (a) air temperature profile and (b) ocean potential temperature profile averaged between 10°S and 10°N.

TOM (at approximately 2.0 hPa). This formulation represents the radiative effect of water vapor and other greenhouse gases (CO_2, O_3, CH_4, and N_2O).

Figure 4 shows how the global-mean surface air temperature, column water vapor amount, and clear-sky greenhouse effect vary with sea ice cover. In the control experiment (100% solar radiation and 355 ppmv CO_2), the clear-sky greenhouse effect ranges from 15 W m^{-2} at the poles to 180 W m^{-2} over the equator, and the global- and annual-mean G is 129 W m^{-2} (Fig. 4c), which is comparable to observations (Raval and Ramanathan 1989). As solar radiation and/or CO_2 concentration is reduced, it is clear that 1) the surface air temperature approximately linearly decreases as the sea ice cover increases, consistent with the prediction in the Goddard Institute for Space Studies (GISS) general circulation model (Stone and Yao 2004); 2) the amount of water vapor and the clear-sky greenhouse effect decline nearly logarithmically as the sea ice cover increases, reflecting the sensitive dependence of the saturated vapor pressure of the water on air temperature, which is consistent with observations (Raval and Ramanathan 1989) and with the simulated results of Voigt and Marotzke (2010). The decrease of the clear-sky greenhouse effect further reduces the air and surface temperatures, enhancing the advance of the sea ice. On the hard Snowball Earth, the global-mean clear-sky greenhouse effect is as low as 22 W m^{-2}, comparable to the results of Le-Hir et al. (2007) and Hu et al. (2011).

In the experiment with 6% less solar radiation and 70 ppmv CO_2 relative to the control experiment, the global-mean clear-sky greenhouse effect decreases by 67 W m^{-2}.

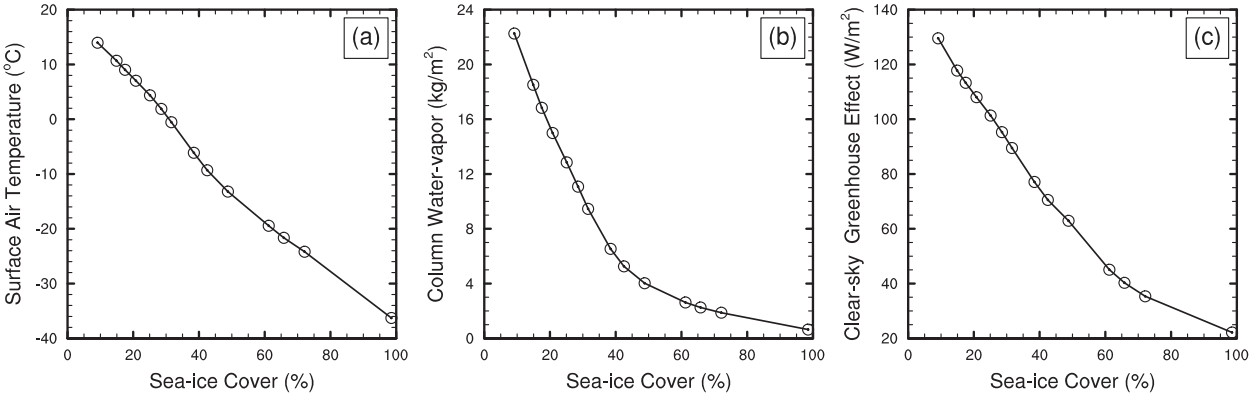

FIG. 4. (a) Global-mean surface air temperature, (b) column-integrated water vapor amount, and (c) clear-sky greenhouse effect as a function of sea ice cover (%).

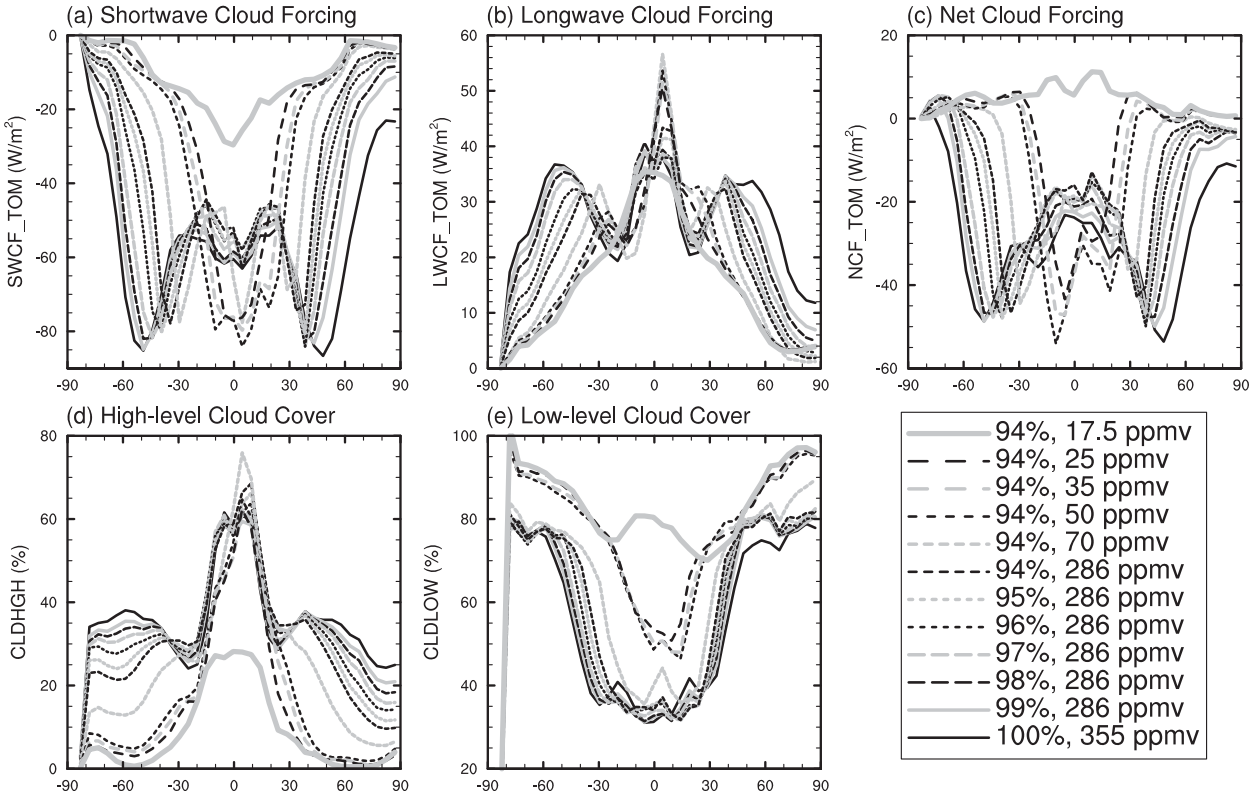

FIG. 5. Zonal-mean (a) cloud shortwave forcing (SWCF), (b) cloud longwave forcing (LWCF), (c) NCF (shortwave plus longwave), (d) high-level cloud fraction (CLDHGH), and (e) low-level cloud fraction (CLDLOW) at TOM in the experiments with different solar radiations and CO_2 concentrations. In the calculations, the land grid cells are excluded.

In the global-mean, the carbon dioxide greenhouse effect decreases by 6.2 W m^{-2} and the greenhouse effect of other gases (CH_4 and N_2O) declines by approximately 0.7 W m^{-2} (Collins et al. 2006a), and thus the decrease of the water vapor greenhouse effect is 60.1 W m^{-2}, which is about twice the external forcing (solar radiation plus CO_2 forcing) reduction (26.7 W m^{-2}). In this calculation, the change of the radiative forcing of CO_2 (longwave plus shortwave, at the top of the model) for each halving of its concentration is approximately -2.66 W m^{-2} (Collins and et al. 2006a).

c. *Cloud radiative feedback*

Cloud can cool the climate by reflecting solar radiation to space, or it may warm the climate by reducing the outgoing terrestrial radiation. The cloud radiative forcings at the TOM and high- and low-level cloud fractions over the ocean and sea ice are shown in Fig. 5.

In the control experiment, the net cloud forcing (NCF_TOM) over the ocean is negative, -34 W m^{-2}, and the longwave cloud forcing (LWCF_TOM) over sea ice is approximately 23 W m^{-2}. It should be mentioned that the cloud shortwave forcing over the sea ice strongly depends on the value of the sea ice/snow albedo because the sea ice/snow albedo is comparable to the cloud albedo. As the solar radiation and/or CO_2 concentration is reduced, it is found that over the sea ice, the high-level (from the level of 400 hPa to the top of the model) cloud fraction decreases owing to the weakness of convection and the decreases in atmospheric water vapor, whereas the low-level (from the surface to the level of 700 hPa) cloud fraction increases because of the increases in atmospheric relative humidity (RH, not shown). The cloud fraction depends on RH and high (low) RH results in more (less) cloud cover. As a result, during the initiation of the Snowball Earth, the cloud longwave forcing over the sea ice decreases, promoting the advance of the sea ice. Over the open oceans, the situation is more complex. When the sea ice line is outside the tropics, the strength of the net cloud forcing (longwave plus shortwave) decreases, mostly owing to decreases in the supply of atmospheric water vapor for the formation of clouds, which inhibits the equatorward advance of the sea ice. However, as the sea ice enters the tropics, the low-level cloud fraction greatly increases because of the enhanced convection accompanied by increases in the strength of the

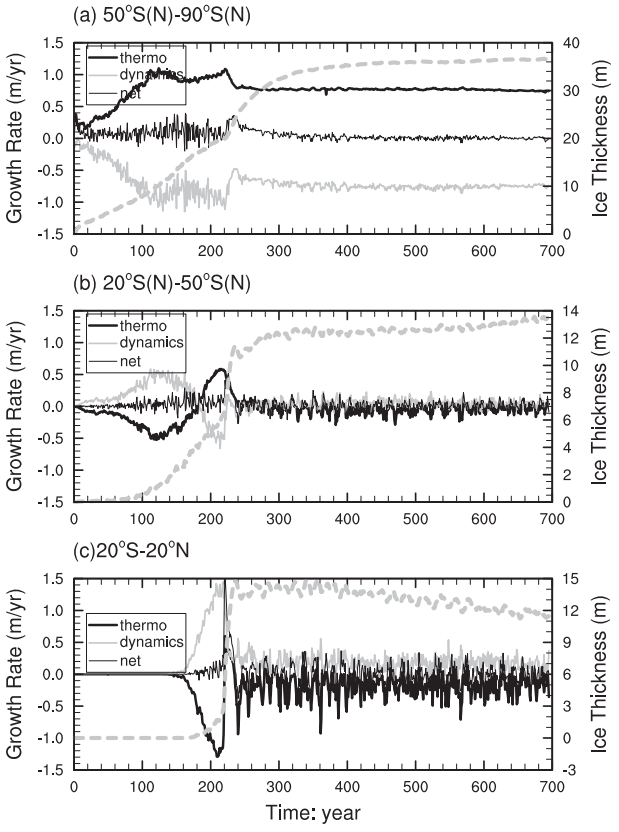

FIG. 6. Ice growth/melting due to thermodynamics (thick black line), dynamics (solid gray line), and net (thin black line) in the experiment with 88% solar radiation and 286 ppmv CO_2, as well as sea ice thickness (gray dashed line, right axis) for different regions: (a) 50°S (N)–90°S (N), (b) 20°S (N)–50°S (N), and (c) 20°S–20°N. Global freezing occurs at the model year 220.

Hadley Cells (see section 3e), which significantly increases the shortwave cloud forcing (negative) and thus promotes sea ice advance. To summarize, the cloud radiative feedback over the sea ice is positive, while over the open water regions it is first negative but becomes positive as the sea ice enters the tropics.

d. Sea ice thermodynamics and dynamics

As shown in Part I, sea ice dynamics may play an important role in the initiation of the Snowball Earth. Without sea ice dynamics, the system will be more reluctant to enter a state of global glaciation. Here, we provide further detail on sea ice dynamics and thermodynamics. The growth/melting of sea ice depends on two distinct contributions, namely, thermodynamics and dynamics, which are illustrated in Fig. 6. In this experiment, the solar radiation is 12% less than the present and the CO_2 concentration is fixed at 286 ppmv. Different latitudinal regions have been individually considered, namely, 50°S (N)–90°S (N), 50°S (N)–20°S (N), and 20°S–20°N.

At high latitudes [50°S (N)–90°S (N)], heat loss from the oceans to the atmosphere supports sea ice increase, and the growth rate itself continues to increase until it reaches approximately 1 m yr^{-1} at model year 120, after which the growth rate remains constant and then abruptly decreases to ~0.7 m yr^{-1} as the ocean becomes completely covered by sea ice at model year 220. The decrease of the sea ice thickness due to equatorward dynamic transport follows the growth rate, and its amplitude is only sightly smaller than the thermodynamic growth rate. Combining these two contributions, the net growth rate is only 0.1 m yr^{-1}, and the ice thickness reaches 24 m as the hard Snowball Earth forms at model year 220.

In the midlatitude region between 20°S (N) and 50°S (N), the contributions of these two influences are opposite: the thermodynamic growth rate is negative, which means sea ice is melting, while the dynamic contribution is positive (less than 0.5 m yr^{-1}), which implies ice transport from high latitudes. The net growth rate of sea ice is less than 0.1 m yr^{-1}. At model year 180, the basal sea ice begins to grow; the area-averaged ice thickness reaches 11 m at model year 220.

For the tropics (20°S–20°N), the sea ice begins to appear at model year 175 because of ice transport from the subtropics, while the thermodynamic contribution is negative, therefore leading to the melting of the sea ice. The area-averaged ice thickness reaches 13.5 m at model year 220.

To clearly display the sea ice transports, three snapshots of the sea ice velocity at model years 90–99, 180–189, and 390–399 are displayed in Fig. 7. It is found that 1) near the ice margins, the annual-average ice drift velocity is about 20 cm s^{-1} (Fig. 7a), comparable to observations in the Norwegian Sea (Barry et al. 1993); and 2) as the sea ice enters the deep tropics, the sea ice velocity significantly increases owing to the large stresses associated with strong tropical trade winds (Fig. 7b). The time-averaged meridional speed near the ice margins is 2 cm s^{-1}—that is, 631 km yr^{-1}—but the net speed of advance of the sea ice fronts is only about 40 km yr^{-1} because most of the advancing ice is melted. Interestingly, in the hard Snowball state, the sea ice in the tropics is about 2.5 m thicker than that at midlatitudes between years 240 and 400, after which the thickness of the tropical ice begins to decrease (Figs. 6, 7c). It should be noted that during the period of integration of this experiment (400 yr), the ocean has yet to reach equilibrium, so that the ice thickness distribution in Fig. 7c is not the final state.

The sea ice growth and melting determines the ocean salinity distribution (Fig. 8). The melting of the sea ice near the ice fronts delivers a large volume of freshwater into the ocean and produces a region with a minimum salinity in each hemisphere (Figs. 8h–j); the salinity in

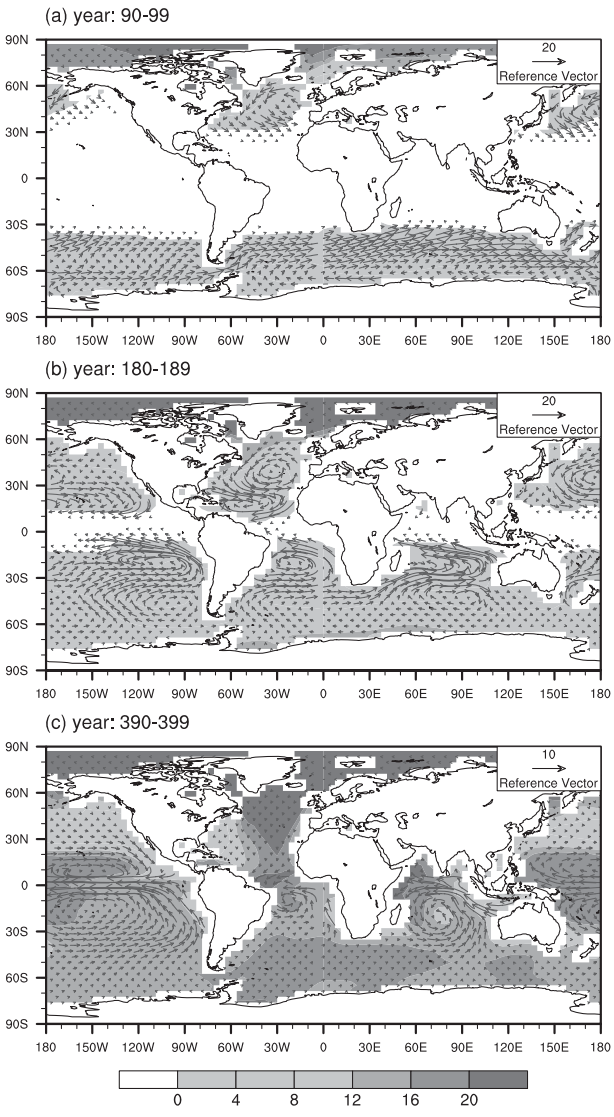

FIG. 7. Ice thickness (shaded, m) and ice velocity (vectors, cm s^{-1}) in the experiment with 88% solar radiation and 286 ppmv CO_2 for three different stages: ice line is poleward of the HCs (years 90–99), ice line has entered the domain of the HCs (years 180–189), and global surface is covered by sea ice/snow (years 390–399). White regions are open seawater or land.

this region may be as low as 23 g kg^{-1}, approximately 30% lower than the global-mean value. Meanwhile, at high latitudes, ice formation salinates the underlying seawater and this high salinity water then sinks into the abyss. Finally, in most parts of the deep ocean, the seawater salinity reaches as high as 35 g kg^{-1}. Moreover, the salinity in the SH is higher than in the NH because the growth rate of sea ice in the SH is greater than in the NH (Fig. 7 of Part I). Of course, over a sufficiently long period of accumulation of snow on the continents, significant ocean water would be contributing to the buildup of continental ice sheets, which would lead to a significant increase in mean ocean salinity. This influence is not captured in the analyses, which we are discussing herein.

e. Dynamics of the Hadley cells

The HCs transport energy from the tropics to the subtropics, weakening the tropical meridional temperature gradient. In the control experiment, the strength of the annual-mean Hadley cells, represented by the absolute value of the maximum atmospheric mass streamfunction, is approximately 98×10^9 kg s^{-1} (Fig. 9). After reducing the solar radiation and/or CO_2 concentration, the Hadley cells intensify, especially in the SH, partly because of the increased meridional temperature gradient (Fig. 10). For instance, in the experiment with a 6% reduction in solar radiation and 70 ppmv CO_2, the equator-to-pole temperature difference increases from 67 to 82 K in the NH and from 46 to 70 K in the SH; as a result, the strength of the Hadley circulation increases to 119×10^9 kg s^{-1} in the NH and to 186×10^9 kg s^{-1} in the SH. Meanwhile, the upward branch of the annual-mean Hadley circulation shifts northward, associated with the northward migration of the ITCZ as mentioned previously (see Fig. 1c). This northward shift has an important effect on the strength of the Hadley circulation. As proposed by Lindzen and Hou (1988), when the thermal equator is displaced off the geographical equator, the winter cell is nonlinearly amplified and the summer cell is weakened. This is the reason why the strength of the Hadley cell in the SH increases approximately 100%–200% while the Hadley cell in the NH remains nearly unchanged in strength (Figs. 9i,j). A further consequence of the decrease in solar radiation/CO_2 concentration is that the Hadley cells become shallower in depth and narrower in width because of the decrease of the tropopause height (Fig. 3), which is one of the factors in determining the extent of the Hadley cells (Held and Hou 1980). Interestingly, the width of the Hadley cells never falls below 20° in latitude (Fig. 9), even on the hard Snowball Earth (Pierrehumbert 2005; Hu et al. 2011; Williams 2006), the principal control on which is, as yet, unclear.

It is important to note that the strength of the Hadley cells determined on the basis of the annual mean pattern [Fig. 9; the analyses of Poulsen and Jacob (2004) and Voigt and Marotzke (2010)] is to some degree misleading, especially for a planet on which the seasonal cycle has a large amplitude (Lindzen and Hou 1988; Pierrehumbert 2005). As shown in Fig. 11, although the strength of the annual-mean HCs (black lines) decreases abruptly as the sea ice fronts approach the equator, the strength of the Hadley cells in January and July (gray lines) is still very high (approximately 450×10^9 kg s^{-1},

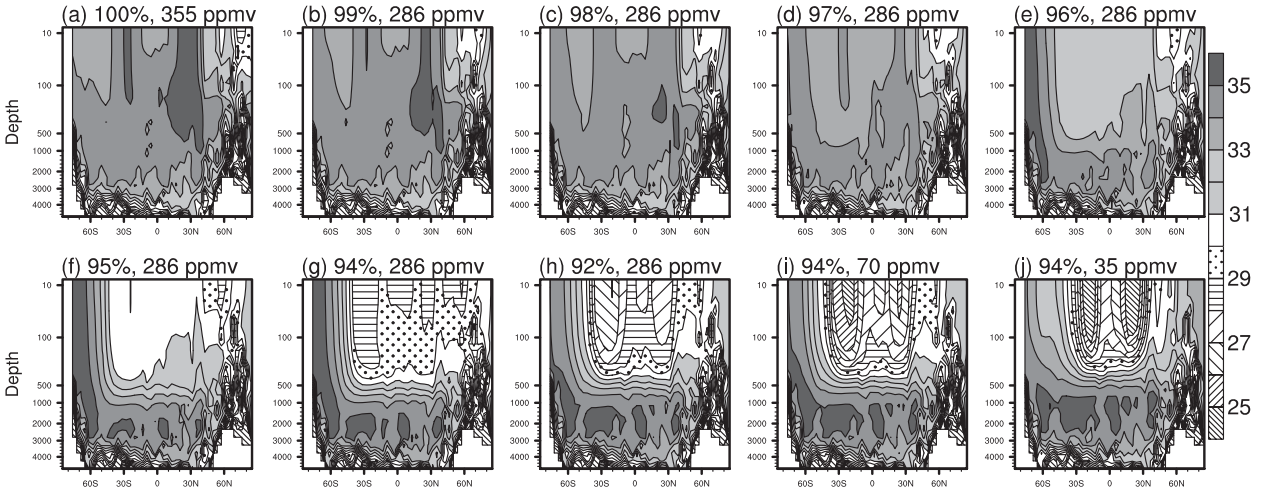

FIG. 8. Ocean salinity (g kg^{-1}) in the experiments with different solar radiations and CO_2 concentrations. solar radiation percentage and carbon dioxide concentration are marked at the top of each panel.

i.e., 4.5 times the present-day level). Therefore, the conclusion of Poulsen and Jacob (2004, p. 10) that "the Hadley circulation collapses prior to complete freezing of the ocean surface, weakening the ice albedo feedback" is misleading. In fact, the Hadley cells are still so strong that very large volumes of relatively cold air are transported from the winter hemisphere to the summer hemisphere, enhancing the influence of the ice albedo feedback.

f. The wind-driven ocean circulations

The wind-driven circulations control the oceanic heat transport in the deep tropics. As demonstrated in Fig. 12, upon reduction in solar radiation and/or atmospheric CO_2 concentration, the southern anticlockwise cell strengthens, the northern clockwise cell remains essentially unchanged, and the center of the two cells shifts northward as the sea ice advances close to the tropics. The intensification of the wind-driven circulations transports more heat to the sea ice fronts, leading to the melting of the advancing sea ice, especially in the SH. Meanwhile, the freshwater provided by sea ice melting increases the ocean stratification, thereby inhibiting vertical convective mixing and weakening the downwelling branch of the wind-driven circulations (Figs. 12h–j). Another significant modification is connected with the

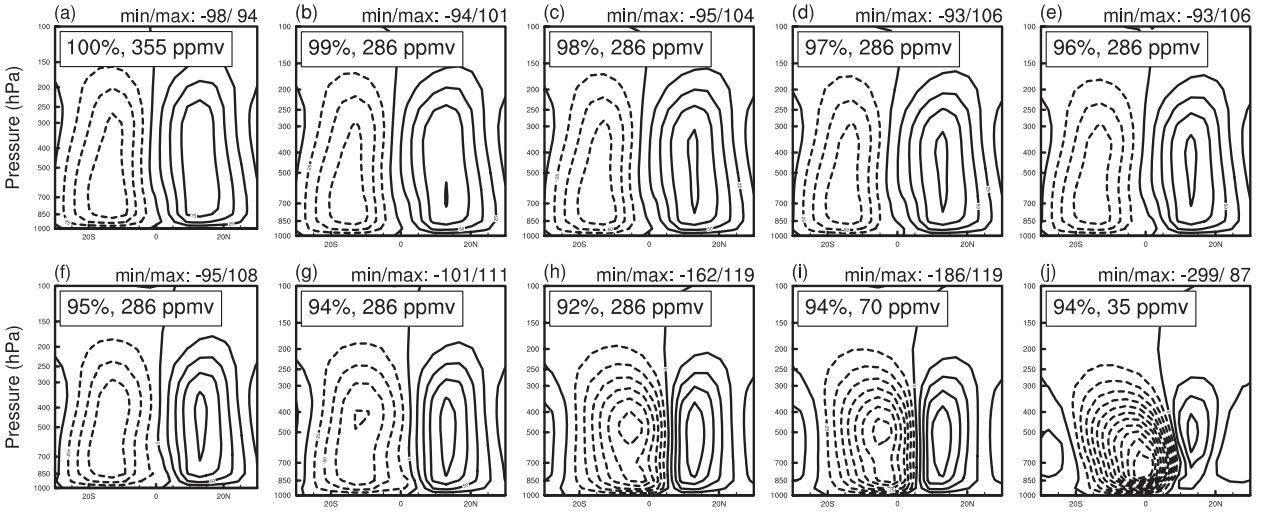

FIG. 9. Annual-mean atmospheric mass streamfunction between 30°S and 30°N (10^9 kg s^{-1}). Solid line denotes clockwise cell; dashed line denotes anticlockwise cell. Solar radiation percentage and carbon dioxide concentration are marked in each panel. Minimum and maximum values are shown at the top of each panel. Contour interval is 25×10^9 kg s^{-1}.

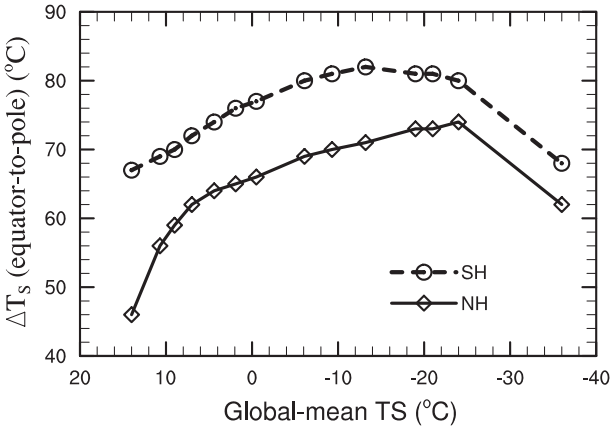

FIG. 10. Annual-mean surface air temperature differences ΔT_S between the "thermal equator" and the pole in the SH and NH. The thermal equator is defined as the location of maximum surface air temperature.

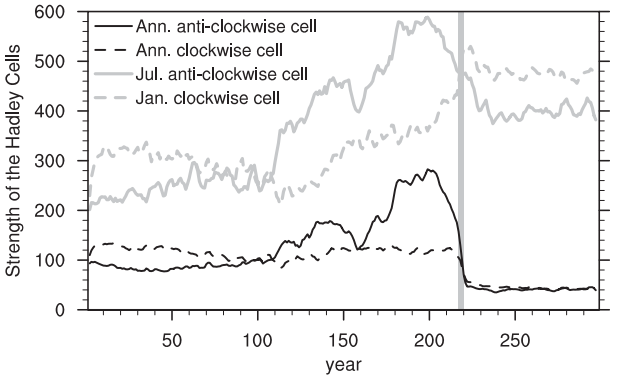

FIG. 11. Time evolution of the strength of HCs (10^9 kg s^{-1}) in January, July, and annual mean (ann.) in the experiment with 88% solar radiation and 286 ppmv CO_2. Vertical gray line represents the time at which global freezing occurs.

weakening of the midlatitude wind-driven circulation in the Southern Ocean, which totally disappears as sea ice advances into this region.

Comparing Figs. 9 and 12, it is clear that the changes in the Hadley cells and the wind-driven circulations are synchronous. In fact, the tropical wind-driven circulations are strongly coupled to the Hadley cells, since the surface branches of both can be thought of as being associated with the Ekman transport arising from the same surface wind stresses (Held 2001). As sea ice advances equatorward, the surface wind stresses increase in the tropics and decrease at mid- and high latitudes (not shown), which is consistent with the changes of both the Hadley cells and the wind-driven circulations.

g. *Thermohaline circulation*

Figure 13 illustrates a series of depictions of the meridional overturning circulation of the Atlantic Ocean as a function of the reduction in solar radiation and/or atmospheric CO_2 concentration. In the control experiment, the strength of the NAMOC is 14.8 Sv (1 Sv $\equiv 10^6$ m^3 s^{-1}), comparable to that observed (Talley et al. 2003). After a 1% reduction in solar radiation and a 69 ppmv reduction in the CO_2 volume mixing ratio, the NAMOC decreases to 8.2 Sv and becomes shallower in depth (shoals), which is accompanied by a southward shift of the region of the most intense deepwater formation. The weakening of the NAMOC amplifies the cooling of the overlying atmosphere at high latitudes of the North Hemisphere; the surface air temperature is about 6 K lower relative to the

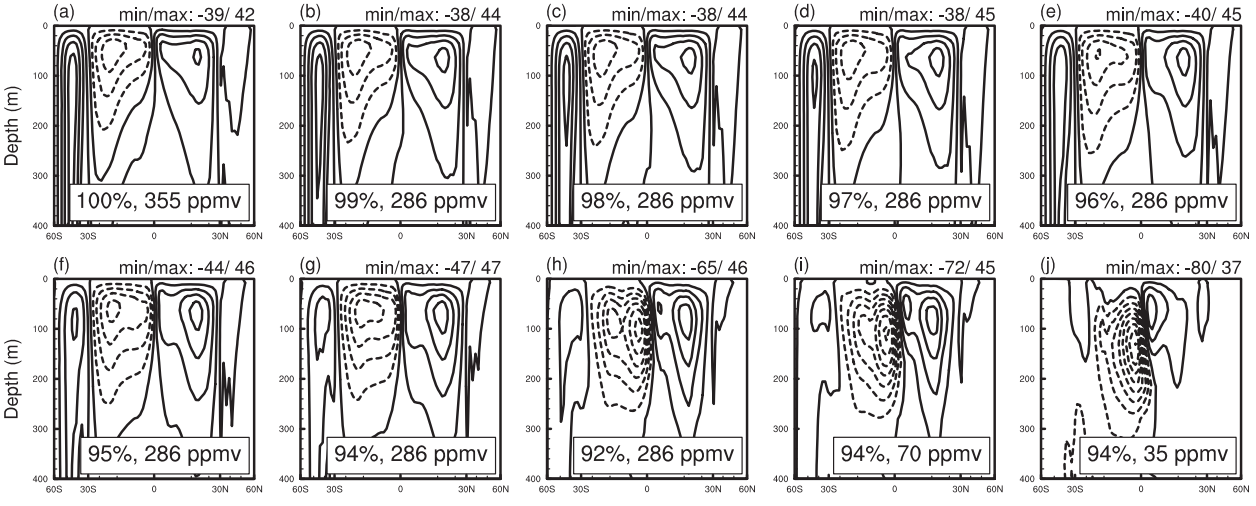

FIG. 12. Annual-mean streamfunction of the zonally integrated meridional overturning circulation above 400 m between 60°S and 60°N. Solar radiation percentage and carbon dioxide concentration are marked in each panel. Minimum and maximum values are shown at the top of each panel. Contour interval is 10 Sv.

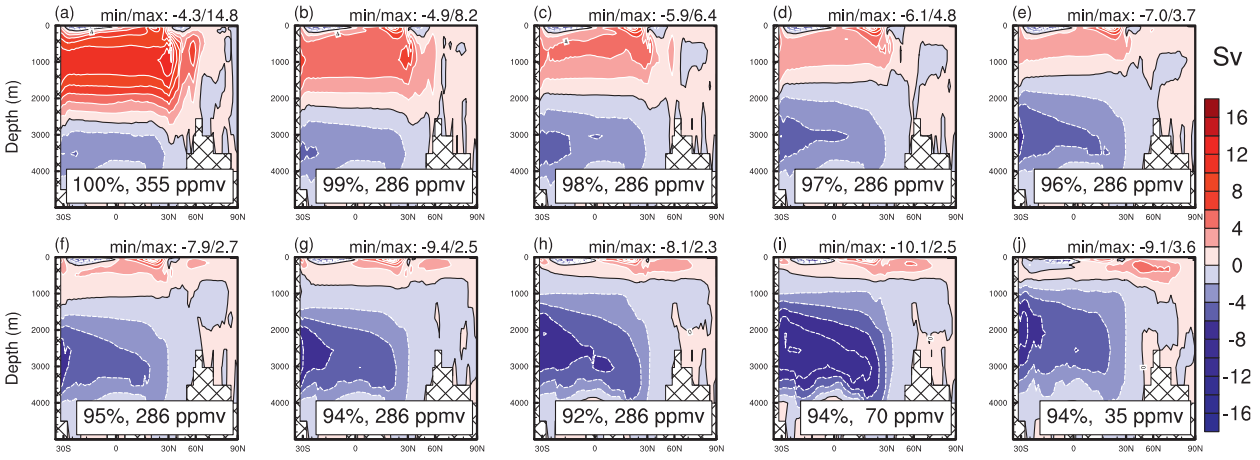

FIG. 13. As in Fig. 12, but for the Atlantic Ocean between the level of 400 m and the bottom of the ocean. Solar radiation percentage and carbon dioxide concentration are marked in each panel. Minimum and maximum values are shown at the top of each panel. Contour interval is 2 Sv.

equivalent latitude of the Southern Hemisphere (Fig. 1b). Meanwhile, the Antarctic Bottom Water cell strengthens and expands to fill a greater depth and extends northward into the Northern Hemisphere, consistent with the results in ECHAM5/MPI-OM (Voigt and Marotzke 2010). These changes are similar to those that accompanying the glacial climate of the Last Glacial Maximum around 21 kyr BP (e.g., Solheim and Peltier 2004), and which we expect to have played a prominent role in the 80 ppmv drawdown of atmospheric CO_2 during Late Cenozoic glacial conditions.

With a further decrease in solar radiation (6% less than the present-day level), the North Atlantic thermohaline circulation collapses entirely and the Antarctic Bottom Water cell comes to occupy almost all of the Atlantic basin, which has been referred to as the ''off mode'' of the Atlantic thermohaline circulation (THC). For the global meridional overturning circulation, the modified system is similar to that in the Atlantic Ocean (not shown). All of these changes imply a reduced northward heat transport and an increased southward heat transport as the system is forced to make the transition into a Snowball state under modern land–sea distribution conditions (see section 3h).

It will be observed that the predicted regime shift of the thermohaline circulation that occurs when the solar luminosity/CO_2 concentration is diminished is simply an exaggerated version of the same ''bipolar seesaw'' shift that is the characteristic of the switch from the modern climate to Last Glacial Maximum climate in response to the cooling due to the imposition of the vast Northern Hemispheric land ice sheets and the accompanying drop in atmospheric carbon dioxide concentration by approximately 80 ppmv (Solheim and Peltier 2004). In both cases the decrease in the strength of the North Atlantic Deep Water (NADW) formation is accompanied by an increase in the rate of formation of Antarctic Bottom Water (AABW). The expansion of Southern Hemispheric and Northern Hemispheric sea ice is associated with a strong influence on the interhemispheric seesaw. Sea ice melting near the ice edge freshens the ocean, while sea ice formation in high latitudes salinates the ocean, both of which effectively increase the salinity difference between the polar regions and the tropics-subtropics. More importantly, the sea ice growth rate at high latitudes of the Southern Hemisphere (poleward of 50°S) is more extreme than that in the equivalent latitudes of the Northern Hemisphere, 0.30 versus 0.15 cm day^{-1} (see Fig. 7 of Part I), the net effect of which results in the salinity of the SH becoming higher than that of the NH. In our analyses based on CCSM3, there is a salinity contrast of ~4 g kg^{-1} between the high latitudes of the two hemispheres (Figs. 8f–j). This interhemispheric salinity contrast provides the buoyancy force needed to drive a pole-to-pole thermohaline circulation that is increasingly dominated by Antarctic Bottom Water (AABW) formation as the solar radiation/CO_2 forcing decreases (Fig. 13). If the ocean salinity distribution were symmetric with respect to the equator, then a pair of equatorially symmetric cells would mostly probably be ensured (Stommel 1961; Bryan 1986). Moreover, the geometry of the ocean basins would considerably modify the pattern of the thermohaline circulation (e.g., Peltier et al. 2004; Enderton and Marshall 2009).

h. Meridional energy transports

The energy transports from the tropics toward the poles result in cooling at low latitudes and warming at high latitudes. Under modern conditions, the radiative

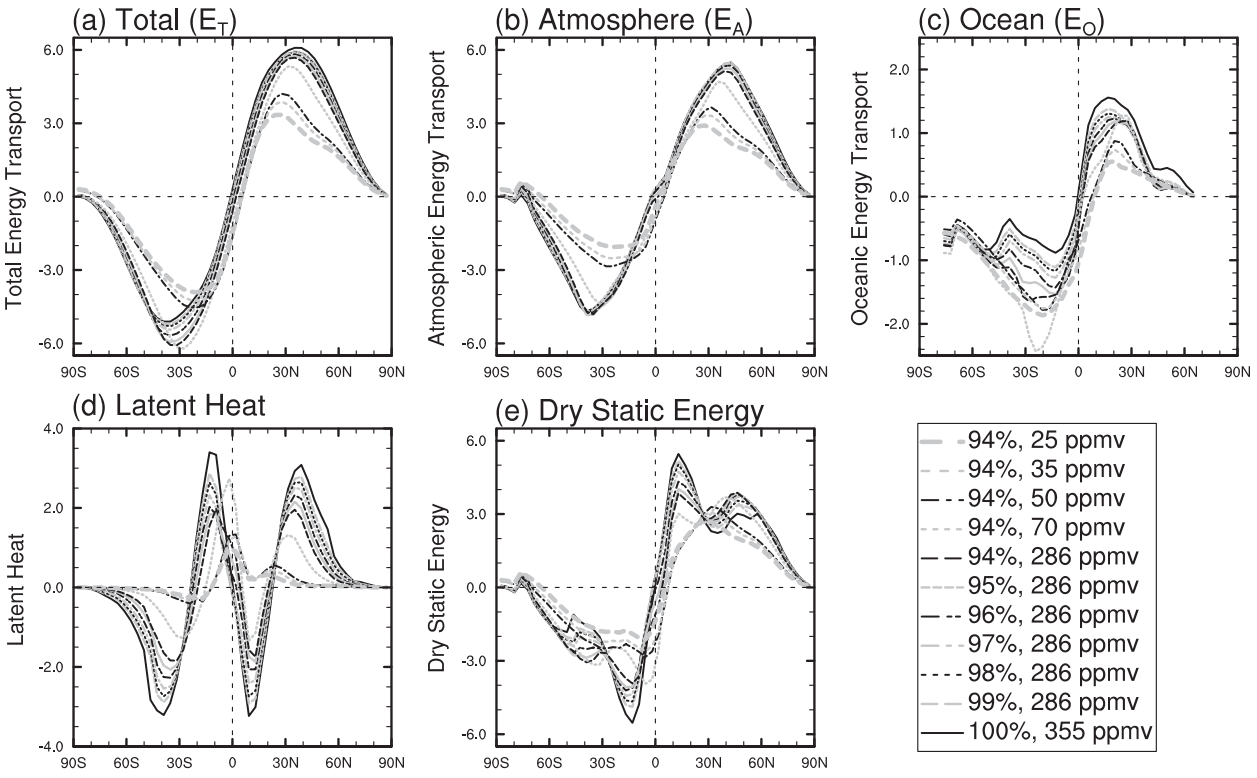

FIG. 14. (a) Annual-mean total meridional energy transport, (b) atmospheric energy transport, and (c) oceanic energy transport; and the contributions of (d) latent heat transport and (e) dry static energy transport to the atmospheric energy transport (PW).

imbalance at the top of the atmosphere averaged over the tropics is approximately 40 W m^{-2} (Hartmann 1994), which is transported poleward by the atmosphere and the ocean. Figure 14 displays the total energy transport E_T, atmospheric heat transport E_A and oceanic heat transport E_O under various solar insolation, and CO_2 concentration. In the control experiment, the E_T peaks at 5.9 PW (4.2 PW, where 1 PW = 10^{15} W) near 37°N (35°S), the E_O peaks at 1.6 PW (1.0 PW) near 18°N (10°S), and the E_A peaks at ~5.0 PW near 40° latitude in both hemispheres, all of which are comparable to the observations discussed in Trenberth and Caron (2001).

After reducing the solar radiation and/or CO_2 concentration, the energy transports show different trends at different regions (out of or in the tropics) and in different periods (before or after the sea ice enters the tropics). When the sea ice remains out of the tropics, it is found that E_T slightly decreases at mid- and high latitudes, mostly arising from the weakened NAMOC, whereas in the tropics between 20°S and 20°N, the energy transports (E_T and E_A) exhibit almost no change. When sea ice enters the tropics, in mid- and high latitudes E_T significantly decreases primarily because of the decline of E_A. In the tropics, however, the changes of E_T and E_A are small, increasing in the SH and decreasing in the NH. In all of these experiments, the oceanic heat transport decreases in the NH and increases in the SH, which is consistent with the transformations of the wind-driven circulations and the thermohaline circulations, as discussed above.

Figures 14d,e show the two components of the atmospheric energy transport: latent heat flux and dry static energy flux. Note that the direction of the latent heat flux is poleward in mid- and high latitudes and equatorward in the tropics, owing to the equatorward transports of moisture in the near-surface branch of the Hadley circulation, while the dry static energy flux is poleward at each latitude. As the solar radiation and/or CO_2 concentration is reduced, the latent heat flux decreases in each latitude because of the reduced water vapor content associated with the colder temperature, meanwhile the dry static energy flux increases in both mid -and high latitudes, owing to the enhanced synoptic eddy activity associated with the increased equator-to-pole temperature gradient (Fig. 10), and decreases in the tropics. As a result, these two contributions almost cancel in mid- and high latitudes and E_A changes only very modestly. However, as the sea ice enters the topics, both the latent heat flux and the dry static energy flux greatly decrease and thus E_A significantly declines in mid- and high latitudes.

As the solar radiation is reduced, for example, by 6%, the solar radiation reduction is 24 W m^{-2} in tropical latitudes and 18 W m^{-2} in mid- and high latitudes, so that less energy is required to be transported poleward (4.2 W m^{-2} if a planetary albedo of 0.3 is assumed, which is about one-tenth of the total energy transport under modern conditions). This is at least part of the reason why the total energy transport slightly decreases at mid- and high latitudes in both hemispheres (Fig. 14a). More importantly, the expansion of the sea ice increases the global-mean planetary albedo and also the meridional albedo gradient. The increase of global-mean planetary albedo decreases the energy that must be transported poleward; however, the increase of the meridional albedo gradient enhances the atmospheric eddy heat transport (not shown).

Stone (1978) argued that for a planet with the earth's radius and tilt of the spin axis with respect to the plane of the ecliptic, the total meridional energy transport would depend on the meridional distribution of the incoming solar radiation and the global-mean planetary albedo, and would be insensitive to the detailed processes of the atmospheric and oceanic circulations. Enderton and Marshall (2009) found Stone's result to be a useful guide to understanding a warm climate without ice, but in a cold climate with polar ice caps, the ice caps can significantly affect the heat transport through the interactions between the ice, atmosphere, and ocean. Our result confirms the suggestion of Enderton and Marshall (2009). Specifically, we find that sea ice formation and melting significantly influence the oceanic thermohaline circulation and thus the meridional oceanic energy transport.

It is worth pointing out that the strength of the Hadley cells increases by a factor of 2–3 as the solar radiation/CO_2 concentration is reduced (see Figs. 9h–j), but the changes of the atmospheric energy transport (latent heat plus dry static energy) in the tropics are very small, slightly increasing in the SH and slightly decreasing in the NH (Fig. 14b). The small changes of atmospheric energy transport occur because of the latent heat, air temperature, and the depth of the Hadley circulation (see Fig. 9) are all reduced, although the strength of the Hadley cells (i.e., meridional wind speed) increases. Atmospheric energy transport is defined as $E_A \equiv \langle \rho LVq + \rho C_p VT + \rho gVZ \rangle$, where ρ is air density, L is the latent heat of condensation, V is meridional wind speed, q is specific humidity, C_p is the specific heat of dry air, T is air temperature, g is gravitational acceleration, and Z is geopotential height (see Pierrehumbert 2002). Angle brackets denote an integral over altitude and an average along a latitude circle. From this definition, one can readily conclude that the small changes of atmospheric energy transports arise from the approximate balance between the decreases of the three quantities (T, q, and Z) and the increase of V.

TABLE 2. NCF at TOM and at SRF in different models. Values are selected as the sea ice cover is ~65% and the sea ice edge reaches ~25°S (N). All of the variables are in W m^{-2}.

Variable	Region	FOAM[a]	ECHAM5/MPI-OM[b]	CCSM3[c]
NCF_TOM	Over ocean		−27	−26
NCF_TOM	Over sea ice		+6	−3
NCF_SRF	Over ocean	−4	−30	−27
NCF_SRF	Over sea ice	+32	+28	+22

[a] Figure 8 of Poulsen and Jacob (2004); experiment was run with 93% solar radiation and 140 ppmv CO_2 under an ideal tropical supercontinent.

[b] Figure 5 of Voigt and Marotzke (2010) and A. Voigt (2011, personal communication); experiment was run with 91% solar radiation and 286 ppmv CO_2 under modern geography and topography.

[c] Figure 5 of this study; experiment was run with 94% solar radiation and 286 ppmv CO_2 under modern geography and topography.

4. Discussion

The coupled ocean–atmosphere models used to investigate the initiation of a Snowball Earth prior to the present study with CCSM3 include FOAM under boundary conditions consisting of an ideal, tropical supercontinent (Poulsen and Jacob 2004), and ECHAM5/MPI-OM under modern geography (Voigt and Marotzke 2010) and under 635-Ma paleogeography (Voigt et al. 2011). As shown in Part I, one of mostly important differences among these models is the sea ice/snow albedo parameterization, which directly influences the strength of the ice albedo feedback. Other differences in cloud radiative forcings and meridional energy transports also affect the forcings required to trigger a Snowball Earth. It is important to understand the extent of these differences.

First, we compare the cloud radiative forcing between FOAM, ECHAM5/MPI-OM, and CCSM3. Table 2 shows the NCFs over ocean and sea ice. It should be noted that in this comparison, the solar radiation and the CO_2 concentration are 93% and 140 ppmv in FOAM, 91% and 286 ppmv in ECHAM5/MPI-OM, and 94% and 286 ppmv in CCSM3, respectively. These differences in external forcings (as well as geography and topography) would also influence the magnitude of the cloud radiative forcing, so that here we consider only differences that are equal to or greater than 10 W m^{-2}. One finds on this basis that the largest difference between these models is in the NCF_SRF. The NCF_SRF over the ocean (negative, cooling effect) in CCSM3 and ECHAM5/MPI-OM is 23 and 26 W m^{-2} stronger, respectively,

TABLE 3. Strength of E_A and E_O in ECHAM5/MPI-OM (Voigt and Marotzke 2010) and CCSM3 (this study) under the present-day geography and topography with a forcing of 94% solar radiation and 286 ppmv CO_2. Peak values of energy transports are listed for the SH and NH, respectively.

Variable	ECHAM5/MPI-OM	CCSM3
E_A (PW)	−4.5, 4.5	−4.7, 5.0
E_O (PW)	−2.0, 1.5	−1.6, 1.2

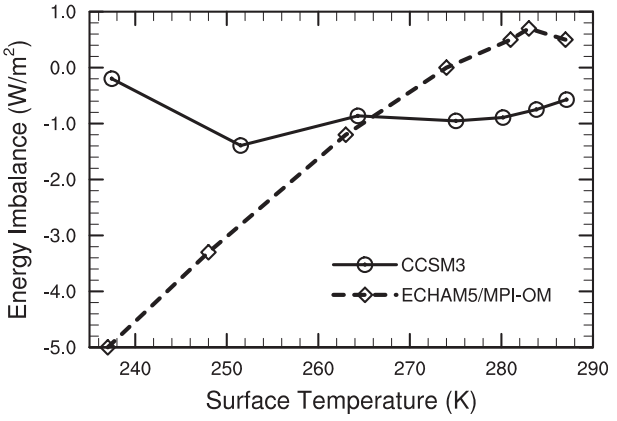

FIG. 15. Energy imbalance as a function of global-mean surface air temperature in CCSM3 (this study) and in ECHAM5/MPI-OM (Voigt et al. 2011). Energy imbalance is defined as the net radiation flux at TOM minus the net heat flux at the surface. Positive values indicate the existence of an artificial energy sink in the atmosphere, and negative values suggest an artificial energy source.

than that in FOAM. Moreover, the NCF_SRF over the sea ice (positive, warming effect) in CCSM3 is 10 W m^{-2} weaker than in FOAM. Based upon this difference, one would expect CCSM3 and ECHAM5/MPI-OM to enter a Snowball Earth state more readily if other conditions were to remain the same.

Next, we examine the differences in the meridional energy transports between CCSM3 and ECHAM5/MPI-OM (Voigt and Marotzke 2010). Both of these models are run under modern geography and topography and with the same external forcing of 94% solar radiation and 286 ppmv CO_2. The final equilibrium sea ice coverage is approximately 20% in ECHAM5/MPI-OM and 30% in CCSM3, although the sea ice albedo in ECHAM5/MPI-OM is much higher than that in CCSM3 (0.75 vs 0.50). Table 3 lists the meridional atmospheric and oceanic energy transports. It is found that the oceanic poleward energy transports in ECHAM5/MPI-OM are greater than in CCSM3 by 0.4 W m^{-2} in the SH and 0.3 W m^{-2} in the NH, corresponding to 2.7 W m^{-2} more energy transported from the tropics to the mid- and high latitudes in ECHAM5/MPI-OM. It is found therefore that the differences in meridional energy transports between ECHAM5/MPI-OM and CCSM3 are much smaller than the differences in the cloud radiative forcing.

As mentioned in Part I, other differences between ECHAM5/MPI-OM and CCSM3 involve the parameterizations of sea ice thickness distribution, the number of sea ice vertical layers, and the sea ice dynamics, which also significantly influence the results. Voigt et al. (2011) have furthermore found that there existed an artificial energy sink/source in the atmosphere module of ECHAM5/MPI-OM and this energy imbalance could be as large as 5 W m^{-2}. We have performed the same analysis based on our CCSM3 simulations and find that the energy imbalance in CCSM3 is less than 1.4 W m^{-2}, much smaller than that in ECHAM5/MPI-OM (Fig. 15).

The most obvious difference between our simulations and those that will be required to represent the actual climate of the Neoproterozoic era is clearly geography. Using ideal and/or realistic geography, various authors have investigated the influences of continental configuration on the formation of the Snowball Earth (Poulsen et al. 2002; Lewis et al. 2003; Donnadieu et al. 2004b; Liu and Peltier 2010; Voigt et al. 2011). Different models have been found to deliver conflicting results. Lewis et al. (2003) and Voigt et al. (2011) found that low-latitude continents are conducive to global glaciation through increasing the planetary albedo and decreasing the content of atmospheric water vapor, as first suggested by Kirschvink (1992). In contrast, Poulsen et al. (2002) found that high-latitude continents cool the polar region and enhance deep-water formation, increasing the oceanic heat transport from low latitudes to high latitudes and cooling the tropical ocean surface, thus facilitating global glaciation. Furthermore, Donnadieu et al. (2004a) suggested that a low-latitude continental configuration would enhance silicate weathering, thereby drawing down the atmospheric CO_2 level and thus promoting the formation of global glaciation. However, Peltier et al. (2007) and Liu and Peltier (2011) argued that a negative feedback involving increased remineralization of organic carbon under increasing cold conditions could prevent the atmospheric CO_2 from decreasing to the low level required to trigger global glaciation. As the surface temperature decreases, the solubility of oxygen in seawater increases, which enhances the remineralization of the dissolved organic carbon and thereby raises the concentration of atmospheric carbon dioxide (Peltier et al. 2007; Rothman et al. 2003).

In the analyses reported here, we find that the land–sea distribution may significantly influence the location of the ITCZ and thus the strength of the Hadley cells and of the wind-driven circulations, as discussed in sections 3e and 3f. If the continents were symmetric with respect to the equator, the Hadley cells and the wind-driven

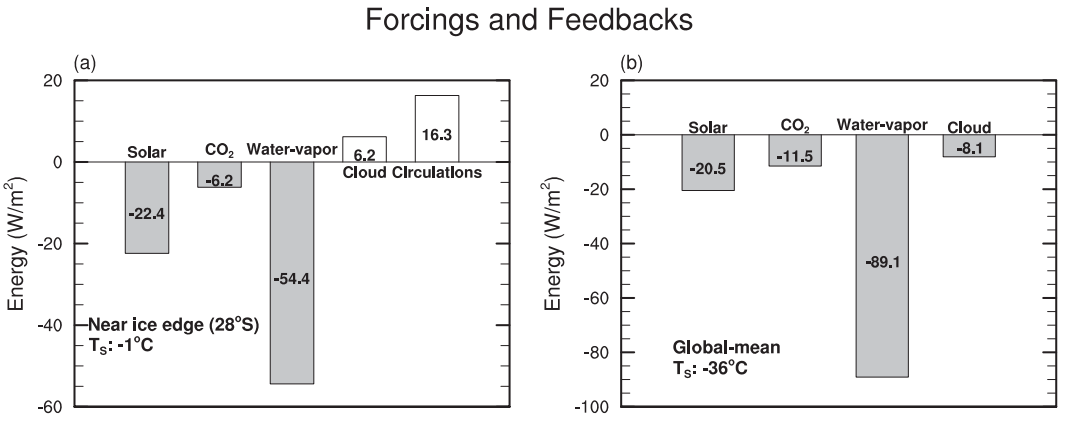

FIG. 16. Forcings (solar radiation and CO_2 forcing) and feedbacks (water vapor, cloud, and atmospheric and oceanic circulations) in (a) a partially ice-covered state in the experiment with 94% solar radiation and 70 ppmv CO_2 (near the ice edge) and (b) a hard Snowball state in the experiment with 94% solar radiation and 17.5 ppmv CO_2 (for global mean) relative to the control experiment with 100% solar radiation and 355 ppmv CO_2. For the cloud feedback, the shortwave forcing strongly depends on the surface snow/sea ice albedo, thus we show only the longwave component at TOM.

circulations might experience a smaller seasonal cycle and would be much weaker than those under the present land–sea distribution. Further simulations will be needed to quantify the effects of the land–sea distribution, not only on the surface albedo and water vapor distribution but also on the atmospheric and oceanic circulations.

5. Summary

Using the fully coupled climate model CCSM3, we have reexamined the transition process from the present-day climate to the extreme cold climate of a modern Snowball Earth. After reducing the solar radiation and/or carbon dioxide concentration, we find that water vapor–temperature feedback significantly enhances ice albedo feedback, such that it is approximately twice as important as the reduction in solar radiation and CO_2 forcing, which leads to the decrease of the amount of atmospheric water vapor (Fig. 16). The cloud feedback is positive over the sea ice and negative over the ocean, however; as the sea ice enters the tropics, the cloud feedback over the ocean becomes positive due to the significant increase in low-level cloud cover. Moreover, the cloud radiative forcing differs largely between different models, and the magnitude of the difference between CCSM3 and ECHAM5/MPI-OM is much greater than that in poleward energy transports. As sea ice advances into low latitudes, the strength of the Hadley cells and the tropical wind-driven circulations significantly increases partly because of the enhanced equator-to-pole temperature gradient and partly because of the northward shift of the ITCZ. This feedback of atmospheric and oceanic circulations acts to inhibit the expansion of sea ice, amounting to an effective heating of approximately 16 W m^{-2} near the ice edge of the SH in the experiment with 94% solar radiation and 70 ppmv CO_2 (Fig. 16). The major determining factors that contribute to the development of a completely ice-covered ocean are therefore the ice/snow albedo feedback (Part I) and the water vapor feedback (this paper). However, in the absence of oceanic heat transports, the earth might very easily succumb to entry into a hard Snowball state, as discussed in Poulsen and Jacob (2004) and Peltier et al. (2004).

The majority of the tropical sea ice originates from mid- and high latitudes via ice transports driven by wind and ocean stresses. Sea ice formation and melting play critical roles in controlling the distribution of ocean salinity. Sea ice melting near the sea ice fronts results in a broad region of minimum salinity in each hemisphere, which strengthens the ocean stratification and thereby weakens the downwelling branch of the wind-driven circulations. In high latitudes, a considerable volume of high-salinity water produced by sea ice formation is injected into the ocean, which strengthens the Antarctic Bottom Water cell, accompanied by increasing southward oceanic heat transport. The North Atlantic Deep Water cell continuously weakens and almost vanishes as sea ice covers the regions of deep-water formation in the North Atlantic and of the wind-driven upwelling in the Southern Ocean. Therefore, on a modern ''soft Snowball'' Earth (open oceans coexists with low-latitude ice-covered continents), the stable pattern of the ocean overturning circulation consists of an interhemispheric and asymmetric cell in which sinking occurs in the Southern Hemisphere and the meridional salinity contrast

due to the sea ice formation and melting provides the buoyancy force required to drive the circulation.

Acknowledgments. We thank the two anonymous referees for their comments. We also thank Yonggang Liu and Alireza Mashayekhi for the deep discussions. J. Yang and Y. Y. Hu are supported by the National Basic Research Program of China (973 Program, 2010CB428606) and by NSF of China under Grants 40875042 and 41025018. J. Yang is partly supported by the Over-sea Study Program for Graduate Students of the China Scholarship Council. W. R. Peltier is supported by the Canadian Foundation for Climate and Atmospheric Sciences and a consortium of Canadian universities and by the NSERC Discovery Grant A9627. The required computations were performed on the SciNet facility at the University of Toronto, which is a component of the Compute Canada HPC platform.

REFERENCES

Barry, R. G., M. C. Serreze, J. A. Maslanik, and R. H. Preller, 1993: The Arctic sea ice-climate system: Observations and modeling. *Rev. Geophys.,* **31,** 397–422.

Baum, S. K., and T. J. Crowley, 2001: GCM response to Late Precambrian (~590 Ma) ice-covered continents. *Geophys. Res. Lett.,* **28,** 583–586.

Bendtsen, J., 2002: Climate sensitivity to changes in solar insolation in a simple coupled climate model. *Climate Dyn.,* **18,** 595–609.

Broccoli, A. J., K. A. Dahl, and R. J. Stouffer, 2006: Response of the ITCZ to Northern Hemisphere cooling. *Geophys. Res. Lett.,* **33,** L01702, doi:10.1029/2005GL024546.

Bryan, F., 1986: High-latitude salinity effects and interhemispheric thermohaline circulations. *Nature,* **323,** 301–304.

Chandler, M. A., and L. E. Sohl, 2000: Climate forcings and the initiation of low-latitude ice sheets during the Neoproterozoic Varanger glacial interval. *J. Geophys. Res.,* **105** (D16), 20 737–20 756.

Collins, W. D., and Coauthors, 2006a: Radiative forcing by well-mixed greenhouse gases: Estimates from climate models in the Intergovernmental Panel on Climate Change (IPCC) Fourth Assessment Report (AR4). *J. Geophys. Res.,* **111,** D14317, doi:10.1029/2005JD006713.

——, and Coauthors, 2006b: The Community Climate System Model version 3 (CCSM3). *J. Climate,* **19,** 2122–2143.

Crowley, T. J., W. T. Hyde, and W. R. Peltier, 2001: CO_2 levels required for deglaciation of a ''near-Snowball'' Earth. *Geophys. Res. Lett.,* **28,** 283–286.

Czaja, A., and J. Marshall, 2006: The partitioning of poleward heat transport between the atmosphere and ocean. *J. Atmos. Sci.,* **63,** 1498–1511.

Donnadieu, Y., Y. Goddéris, G. Ramstein, A. Nédeléc, and J. Meert, 2004a: A 'snowball Earth' climate triggered by continental break-up through changes in runoff. *Nature,* **428,** 303–306, doi:10.1038/nature02.

——, G. Ramstein, F. Fluteau, D. Roche, and A. Ganopolski, 2004b: The impact of atmospheric and oceanic heat transports on the sea-ice-albedo instability during the Neoproterozoic. *Climate Dyn.,* **22,** 293–306.

Enderton, D., and J. Marshall, 2009: Explorations of atmosphere–ocean–ice climates on an aquaplanet and their meridional energy transports. *J. Atmos. Sci.,* **66,** 1593–1611.

Goodman, J. C., 2006: Through thick and thin: Marine and meteoric ice in a ''Snowball Earth'' climate. *Geophys. Res. Lett.,* **33,** L16701, doi:10.1029/2006GL026840.

——, and R. T. Pierrehumbert, 2003: Glacial flow of floating marine ice in ''Snowball Earth.'' *J. Geophys. Res.,* **108,** 3308, doi:10.1029/2002JC001471.

Hartmann, D. L., 1994: *Global Physical Climatology*. Academic Press, 411 pp.

Held, I. M., 2001: The partitioning of the poleward energy transport between the tropical ocean and atmosphere. *J. Atmos. Sci.,* **58,** 943–948.

——, and A. Y. Hou, 1980: Nonlinear axially symmetric circulations in a nearly inviscid atmosphere. *J. Atmos. Sci.,* **37,** 515–533.

Hu, Y. Y., J. Yang, F. Ding, and W. R. Peltier, 2011: Model-dependence of the CO_2 threshold for melting the hard Snowball Earth. *Climate Past,* **7,** 17–25.

Hyde, W. T., T. J. Crowley, S. K. Baum, and W. R. Peltier, 2000: Neoproterozoic 'Snowball Earth' simulations with a coupled climate/ice-sheet model. *Nature,* **405,** 425–429.

Jenkins, G. S., and S. R. Smith, 1999: GCM simulation of Snowball Earth conditions during the Late Proterozoic. *Geophys. Res. Lett.,* **26,** 2263–2266.

Kirschvink, J. L., 1992: Late Proterozoic low-latitude global glaciation: The Snowball Earth. *The Proterozoic Biosphere,* J. W. Schopf and C. Klein, Eds., Cambridge University Press, 51–52.

Le-Hir, G., G. Ramstein, Y. Donnadieu, and R. T. Pierrehumbert, 2007: Investigating plausible mechanisms to trigger a deglaciation from a hard Snowball Earth. *C. R. Geosci.,* **339,** 274–287.

Lewis, J. P., A. J. Weaver, S. T. Johnston, and M. Eby, 2003: Neoproterozoic ''Snowball Earth'': Dynamic sea ice over a quiescent ocean. *Paleoceanography,* **18,** 1092, doi:10.1029/2003PA000926.

——, ——, and M. Eby, 2007: Snowball versus Slushball Earth: Dynamic versus nondynamic sea ice? *J. Geophys. Res.,* **112,** C11014, doi:10.1029/2006JC004037.

Lindzen, R. S., and A. Y. Hou, 1988: Hadley circulations for zonally averaged heating centered off the equator. *J. Atmos. Sci.,* **45,** 2416–2427.

Liu, Y., and W. R. Peltier, 2010: A carbon cycle coupled climate model of Neoproterozoic glaciation: Influence of continental configuration on the formation of a ''soft Snowball.'' *J. Geophys. Res.,* **115,** D17111, doi:10.1029/2009JD013082.

——, and ——, 2011: A carbon cycle coupled climate model of Neoproterozoic glaciation: Explicit carbon cycle with stochastic perturbations. *J. Geophys. Res.,* **116,** D02125, doi:10.1029/2010JD015128.

Micheels, A., and M. Montenari, 2008: A Snowball Earth versus a Slushball Earth: Results from Neoproterozoic climate modeling sensitivity experiments. *Geosphere,* **4,** 401–410.

Peltier, W. R., L. Tarasov, G. Vettoretti, and L. P. Solheim, 2004: Climate dynamics in deep time: Modeling the ''Snowball bifurcation'' and assessing the plausibility of its occurrence. *The Extreme Proterozoic: Geology, Geochemistry and Climate, Geophys. Monogr.,* Vol. 146, Amer. Geophys. Union, 107–124.

——, Y. Liu, and J. W. Crowley, 2007: Snowball Earth prevention by dissolved organic carbon remineralization. *Nature,* **450,** 813–818.

Pierrehumbert, R. T., 2002: The hydrologic cycle in deep-time climate problems. *Nature,* **419,** 191–198.

——, 2004: High levels of atmospheric carbon dioxide necessary for the termination of global glaciation. *Nature,* **429,** 646–649.

——, 2005: Climate dynamics of a hard Snowball Earth. *J. Geophys. Res.,* **110,** D01111, doi:10.1029/2004JD005162.

——, D. S. Abbot, A. Voigt, and D. Koll, 2011: Climate of the Neoproterozoic. *Annu. Rev. Earth Planet. Sci.,* **39,** 417–460.

Pollard, D., and J. F. Kasting, 2004: Climate-ice sheet simulations of Neoproterozoic glaciation before and after collapse to Snowball Earth. *The Extreme Proterozoic: Geology, Geochemistry and Climate, Geophys. Monogr.,* Vol. 146, Amer. Geophys. Union, 91–105.

——, and ——, 2005: Snowball Earth: A thin-ice solution with flowing sea glaciers. *J. Geophys. Res.,* **110,** C07010, doi:10.1029/2004JC002525.

Poulsen, C. J., and R. L. Jacob, 2004: Factors that inhibit Snowball Earth simulation. *Paleoceanography,* **19,** PA4021, doi:10.1029/2004PA001056.

——, R. T. Pierrehumbert, and R. L. Jacob, 2001: Impact of ocean dynamics on the simulation of the Neoproterozoic ''Snowball Earth.'' *Geophys. Res. Lett.,* **28,** 1575–1578.

——, R. L. Jacob, R. T. Pierrehumbert, and T. T. Huynh, 2002: Testing paleogeographic controls on a Neoproterozoic Snowball Earth. *Geophys. Res. Lett.,* **29,** 1515, doi:10.1029/2001GL014352.

Raval, A., and V. Ramanathan, 1989: Observational determination of the greenhouse effect. *Nature,* **342,** 758–761.

Roe, G. H., and M. B. Baker, 2010: Notes on a catastrophe: A feedback analysis of Snowball Earth. *J. Climate,* **23,** 4694–4703.

Romanova, V., G. Lohmann, and K. Grosfeld, 2006: Effect of land albedo, CO_2, orography, and oceanic heat transport on extreme climates. *Climate Past,* **2,** 31–42.

Rose, B. E. J., and J. Marshall, 2009: Ocean heat transport, sea ice, and multiple climate states: Insights from energy balance models. *J. Atmos. Sci.,* **66,** 2828–2843.

Rothman, D. H., J. M. Hayes, and R. E. Summons, 2003: Dynamics of the Neoproterozoic carbon cycle. *Proc. Natl. Acad. Sci. USA,* **100,** 8124–8129.

Solheim, L. P., and W. R. Peltier, 2004: The climate of the Earth at Last Glacial Maximum: Statistical equilibrium state and a mode of internal variability. *Quat. Sci. Rev.,* **23,** 335–357.

Stommel, H., 1961: Thermohaline convection with two stable regimes of flow. *Tellus,* **13,** 224–230.

Stone, P. H., 1978: Constraints on dynamical transports of energy on a spherical planet. *Dyn. Atmos. Oceans,* **2,** 123–139.

——, and M. S. Yao, 2004: The ice-covered Earth instability in a model of intermediate complexity. *Climate Dyn.,* **22,** 815–822.

Tajika, E., 2003: Faint young sun and the carbon cycle: Implication for the Proterozoic global glaciations. *Earth Planet. Sci. Lett.,* **214,** 443–453.

Talley, L., J. Reid, and P. Robbins, 2003: Data-based meridional overturning streamfunctions for the global ocean. *J. Climate,* **16,** 3213–3224.

Trenberth, K. E., and J. M. Caron, 2001: Estimates of meridional atmosphere and ocean heat transports. *J. Climate,* **14,** 3433–3443.

Voigt, A., and J. Marotzke, 2010: The transition from the present-day climate to a modern Snowball Earth. *Climate Dyn.,* **35,** 887–905, doi:10.1007/s00382-009-0633-5.

——, D. S. Abbot, R. T. Pierrehumbert, and J. Marotzke, 2011: Initiation of a Marinoan Snowball Earth in a state-of-the-art atmosphere-ocean general circulation model. *Climate Past,* **7,** 249–263.

Williams, G. P., 2006: Circulation sensitivity to tropopause height. *J. Atmos. Sci.,* **63,** 1954–1961.

Yang, J., W. R. Peltier, and Y. Y. Hu, 2012: The initiation of modern ''soft Snowball'' and ''hard Snowball'' climates in CCSM3. Part I: The influence of solar luminosity, CO_2 concentration, and the sea ice/snow albedo parameterization. *J. Climate,* **25,** 2711–2736.